RICE UNIVERSITY

Saturation Effects in Photoassociation Spectroscopy of ^{86}Sr

by

Pascal Gerry Mickelson

A Thesis Submitted
in Partial Fulfillment of the
Requirements for the Degree

Master of Science

Approved, Thesis Committee:

Thomas C. Killian, Chair
Assistant Professor of Physics and Astronomy

Randall G. Hulet
Fayez Sarofim Professor of Physics of Physics and Astronomy

Daniel M. Mittleman
Associate Professor of Electrical and Computer Engineering

Houston, Texas

APRIL 2006

ABSTRACT

Saturation Effects in Photoassociation Spectroscopy of ^{86}Sr

by

Pascal Gerry Mickelson

This work describes intensity saturation of photoassociative transitions of ^{86}Sr at the quantum mechanical unitarity limit. The saturation behavior, which results in a roll-over of the photoassociation rate for intensities greater than the saturation intensity, features interesting physics. Unlike other photoassociation spectroscopy (PAS) experiments, photoassociation occurs in a magneto-optical trap operating on the narrow dipole-forbidden transition at 689 nm. A laser red-detuned from the principal atomic transition at 461 nm by as much as 1300 GHz induces the photoassociation of ground state atoms to excited molecular states. Our previous studies [1] suggest that some of the PAS transitions for ^{86}Sr are sensitive to the intensity of the laser. This work delves more deeply into these high intensity PAS effects, a subject that has not, to our knowledge, been studied experimentally for alkaline-earth atoms.

Acknowledgments

I could not have written this thesis without the aid of many people. Many thanks go to: my advisor, Tom Killian, for his insightful critiques and bountiful patience. The other members of my committee, Randy Hulet and Dan Mittleman, for freely giving of their time and knowledge. My colleagues in the Killian lab for contributing their aid and humor during the many stages of the thesis-writing process. My friends in disparate parts of the world for distracting me when I need distraction. And, most of all, my family for their unwavering love and support whatever my decisions may be and however infrequently I may call them.

Contents

Illustrations

Chapter 1

Introduction

This thesis discusses the experiment and analysis that demonstrate saturation due to the unitarity limit of molecular transitions in photoassociation spectra. Work leading up to this conclusion allows the determination of the scattering length of the second most abundant bosonic isotope of strontium, ^{86}Sr, also via photoassociation spectroscopy (PAS). Like all PAS experiments, this work relies on ultracold atoms and tunable narrow-band lasers to excite molecular transitions. Unlike other PAS experiments, however, photoassociation occurs in a magneto-optical trap (MOT) operating on the narrow dipole-forbidden transition at 689 nm. Metcalf and van der Straten's book, Laser Cooling and Trapping [2], describes many of the techniques used in this experiment.

1.1 Laser Cooling and Trapping

Any discussion of ultracold neutral atoms includes a section on laser cooling; that is, the use of light to affect the motion of atoms. In 1975, Hänsch and Schawlow [3] and Wineland and Dehmelt [4] concurrently proposed that the scattering of light by atoms could be used to cool a gas. In its simplest form, the momentum associated with radiation nearly-resonant with the atomic transition frequencies imparts a force to atoms. The absorption of light by the atoms is frequency-dependent, and hence velocity-dependent, because the atoms see a Doppler shift in the frequency from their

motion relative to the laser, which is fixed in the laboratory frame. Provided the light is red-detuned, the shift in the frequency means atoms traveling opposite the direction of the laser will preferentially absorb light from that direction. Because spontaneous emission occurs isotropically, the net momentum change of the atoms is in the direction of the laser.

Once atoms lose momentum, however, they fall out of resonance with the laser beam. In the early 1980s, William Phillips' group at NIST [5, 6] overcame this problem via the Zeeman slowing technique which added a magnetic field gradient tailored to keep the atoms in resonance with the counter-propagating laser as they were cooled. His group managed to slow Na atoms to near rest with respect to the laboratory frame. Later that year, Phillips [7] and Steven Chu et al. [8] successfully achieved atom cooling in three dimensions using a configuration of six counter-propagating, orthogonal laser beams all intersecting at the same point. However, because there is no position-dependent force in this set-up, the sample is simply known as "optical molasses" where cooled atoms are merely slowed and not actually trapped.

Finally, in 1987, Raab et al. [9] first demonstrated the arrangement of counter-propagating laser beams and in-homogeneous magnetic field now known as a magneto-optical trap (MOT). A MOT makes use of an in-homogeneous magnetic field to establish the position-dependent force missing from optical molasses, thus enabling simultaneous cooling and trapping of atoms. The trapping works by taking advantage of the Zeeman splitting of the energy levels of an atom. For a simple two-level system, which is a reasonable approximation for many transitions in various atomic species, the transition will have three Zeeman components that are sensitive to different polarization. The further an atom is from the center of the trap where the field is zero, the stronger the splitting of the energy levels. Using circularly polarized

light in one direction and oppositely circularly polarized light in the other direction, atoms will preferentially absorb light from one polarization, thus creating the position-dependent force required for the MOT. Since its development, the MOT has become the workhorse of experiments with ultracold neutral atoms.

1.2 Studying Cold Collisions

With the firm foundation these experimental techniques allow, work in ultracold physics has blossomed in the last twenty years. In particular, photoassociation spectroscopy, one technique used to study collisions between ultracold atoms, has been the subject of fruitful research. Laser-induced photoassociation was first suggested by Thorsheim, Weiner, and Julienne in a 1987 paper [10] as a technique that could uniquely take advantage of new atom cooling techniques. Photoassociation had previously been observed [11], but unlike that earlier work, laser-induced photoassociation of ultracold atoms provides high enough resolution to observe individual rotational or vibrational transitions [12, 13].

More recent theoretical work on PAS has examined the effect of more intense light fields on photoassociation line shapes [14, 15]. As intensity effects were less well understood, earlier studies of PAS occurred for a low intensity regime where perturbative treatments of photoassociation remain valid. Nevertheless, increasing the light intensity into the saturation regime is a useful technique for modifying photoassociation line shapes. In recent years, experimentalists have studied the intensity dependence of photoassociation in quantum degenerate gases of ^{7}Li [16] and Na [17], in a mixture of ^{6}Li and ^{7}Li [18], in 1D for Na [19], and in an optical dipole trap for Cs dimers [20].

As evidenced by this list, many PAS experiments study group I elements from

the periodic table, the so-called alkali metals. With easily accessible transitions in the visible wavelength regime, the alkali metals were the first atoms to be cooled and trapped. As such, they were the first, obvious target for PAS [21]. However, the group II alkaline-earth elements are also suitable targets and, in fact, are appealing subjects for PAS because they lack hyperfine structure, making for simpler systems with which to test cold collision theory [22]. Interest in alkaline-earth atoms also results because they have narrow optical resonances, resulting from dipole-forbidden transitions between triplet and singlet states, that could be used as improved frequency standards. Finally, laser-cooling on these narrow transitions could yield a much-desired, all-optical path to quantum degeneracy [23, 24].

Photoassociation experiments on calcium [25, 26] and strontium [27, 1] have greatly aided the study of cold collisions in alkaline-earth atoms. In particular, both experiments have yielded estimates of the scattering length for their respective elements. However, to date, neither experiment has closely examined saturation effects at high intensities.

The focus of this work is on these high intensity effects in photoassociation of strontium, and the quantum mechanical unitarity limit turns out to be important for these studies. The unitarity limit occurs because the probability of a scattering event cannot exceed unity. The probability of scattering nominally increases with the intensity, but it must saturate as it approaches unity because doing otherwise would be unphysical. In this work, the saturation of molecular transitions is likely due to this quantum mechanical unitarity limit. Furthermore, the behavior of the saturation curve with increasing intensity properly reflects that of a resonant scattering process rather than a two level bound-bound transition.

In the previous studies of strontium [27, 1], saturation effects were neglected because the quantitative analysis applied to regions unaffected by saturation. However,

it was clear that data in other areas was less well treated. Understanding how saturation occurs allows for a more accurate and quantitative treatment of the subset of the data from those previous studies and reveals interesting physics.

Before confronting the topic of saturation at high intensity, several relevant topics must be discussed. The remainder of this chapter consists of a primer for photoassociation. The second chapter deals with experimental details such as how strontium is trapped and cooled and how photoassociation transitions are excited. The third chapter delves into the analysis of photoassociation spectra before arriving at the discussion of high intensity effects.

1.3 Introduction to Photoassociation

Before launching into the particulars of this research, it will be useful to describe the phenomenon of photoassociation in some detail. Thus far, the term has been used without definition.

On the most fundamental level, photoassociation is the process whereby two atoms interact in the presence of light to form a molecule. Figure 1.1 depicts this process. The atoms begin in an unbound ground state, the lower curve, and end up in an excited bound molecular state, the upper curve. The frequency of the applied light field determines which molecular state is excited. The internuclear separation (R) between the colliding atoms is the horizontal scale while the energy of the two atoms is the vertical scale.

At long range, the potentials adopt the form of C_n/R^n where the C_n coefficients depend on the specific types of interactions possible between the atoms. For example, the ground state potential, along which the two atoms interact, is described by the C_6 coefficient which results from van der Waals interactions. Meanwhile, the C_3/R^3

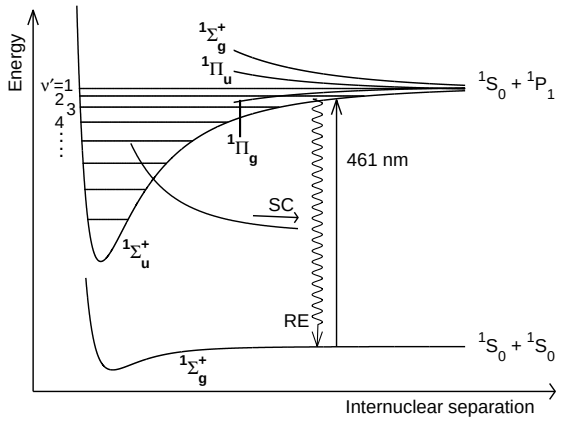

Figure 1.1 : A schematic of photoassociation showing molecular levels (labeled ν) and photoassociative transitions. Atoms interacting along the ground state potential, $^1\Sigma_g^+$, absorb a photon at the frequency corresponding to the energy difference between the ground state and one of the bound levels inside the molecular potential, $^1\Sigma_u^+$. The molecule formed by this process is in an excited state and may radiatively decay to two ground state atoms with enough kinetic energy to escape the trap. This process is called radiative escape (RE). Alternatively, the molecular state may decay to bound levels of the molecular ground state in a process known as state-change (SC). Both processes lead to the loss of atoms from the trap, the experimental "signature" of photoassociation.

form of the excited state potential arises from the atomic transition dipole matrix element. In the molecular excited state, each atom is in a super-position between the $^1P_1$ atomic excited state and the $^1S_0$ atomic ground state. In contrast, the short range potential (small R) is more complicated due to interactions involving the atoms' electron clouds which must be treated fully quantum mechanically. Theorists employ *ab initio* calculations to obtain potentials valid for a particular range of internuclear separation.

The most prominent molecular potential shown in Fig. 1.1, $^1\Sigma_u^+$, contains bound energy levels. However, other molecular potentials exist, such as $^1\Sigma_g^+$ or $^1\Pi_u$ in the

figure. Some of them are repulsive potentials and contain no bound states to excite to. Others may contain bound states, but are inaccessible due to selection rules.

Coupling between the ground state and the excited molecular state is most likely to occur at the Condon point of the bound excited state. Classically, the Condon point is the turning point of the particle in the potential, so it spends more time in that region. Quantum mechanically, the Condon point corresponds to the lobe of the wave function. The overlap integral between the ground and excited states is greatest at that point, making the transition most probable in that region. Either way, the frequency of the transition in question is the difference between the total energy in the ground state and the energy of the particular bound excited state. If the light is not resonant (or nearly-resonant) with the transition, then that particular molecular transition will not be excited. The strength of the transition is proportional to the incident light intensity and the amount of overlap between the ground and excited state wave functions.

Once the atoms are in the excited state, molecules can decay via two processes: radiative escape or state-change. In radiative escape (RE), the molecule dissociates to two ground state atoms at a smaller internuclear separation than it started at. In a state-changing collision (SC), the molecule will decay to bound levels of the ground molecular state, also at a smaller internuclear separation than the location of the original photoassociation. Both RE and SC are loss channels for the trap. In RE, the dissociated atoms gain enough kinetic energy to be ejected from the MOT, and in SC, molecules are not usually trapped by the MOT which only traps ground state atoms. The loss of atoms from the trap, therefore, is the characteristic of photoassociation to look for.

Exciting these resonances via photoassociation yields three main types of information. First, collision energies and intensity effects are determined from the line shape

of individual transitions. Second, by varying the frequency of the laser, it is possible to selectively excite the various resonances in the bound molecular state to obtain a photoassociation spectrum for a broad range of detuning. The full spectrum says much about the location of bound levels in the excited state and determines other excited state parameters. Third, the variation in the strength of transitions yields information about the ground state potential, the wave function of the free ground state atoms, and the s-wave scattering length, which characterizes the strength of the atom interactions.

Previous work done in this research group has, loosely-speaking, yielded information from the second [27] and third [1] categories. The current work continues these photoassociation studies by examining the effect of high intensity on the molecular transition rates, a characteristic of the first category. The following chapters will examine the ideas presented here in the context of strontium and prior work done by this lab.

Chapter 2

Experimental Details

Ultracold atoms and tunable narrow-band lasers underlie all of the experiments that we do. In fact, without them, a phenomenon like photoassociation would be unobservable. In the first section of this chapter on experimental methods, I will describe the steps necessary to achieve temperatures as low as a few μK, while, in the second section, I will discuss the photoassociation experiments underlying the studies described in Chapter 3.

2.1 Making Atoms Cold

The experiment begins with atoms in a magneto-optical trap operating on the 461 nm, $^1S_0$-$^1P_1$ transition of strontium as described in [23, 27]. Figure 2.1 shows which energy levels are connected by this transition, and Fig. 2.2 illustrates the cooling scheme which is used. The two isotopes studied, ^{86}Sr and ^{88}Sr, are separately trappable because the $^1S_0$-$^1P_1$ transitions in each are separated by 163.8 MHz [28], and the laser is readily tunable over this range. In the blue MOT, there are typically 70 million ^{86}Sr atoms and 250 million ^{88}Sr atoms at a temperature of about 2 mK for both isotopes.

Next, the blue MOT is turned off, and another MOT, operating on strontium's 689 nm, $^1S_0$-$^3P_1$, intercombination line, is used to further cool the atoms. The red MOT's beams, each with a diameter of 2 cm and an intensity ranging from 400

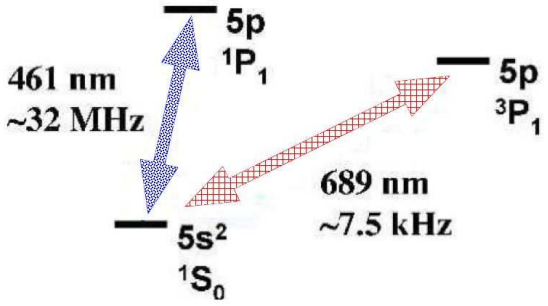

Figure 2.1 : An energy level diagram for strontium shows selected levels. The 461 nm transition is the transition on which the blue MOT operates as well as the transition on which photoassociation is studied. The red MOT operates on the narrow 689 nm transition and cools atoms to temperatures as low as a few μK.

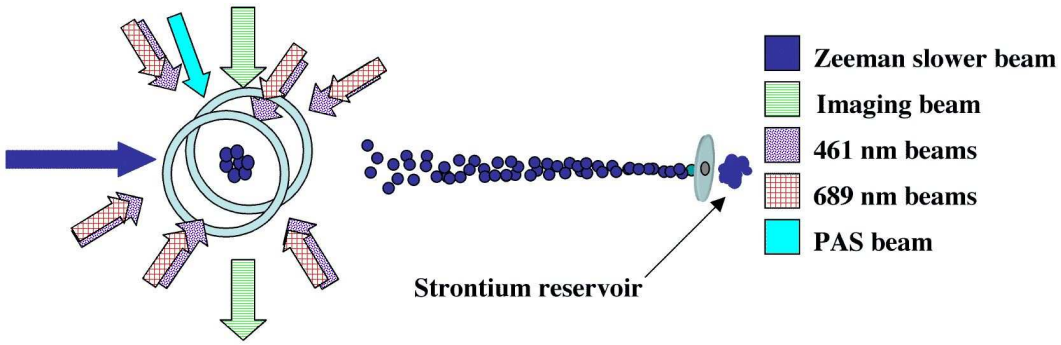

Figure 2.2 : All stages of cooling are shown in this cartoon depicting the trapping and cooling of strontium. Strontium atoms from the oven are initially slowed by the Zeeman beam in the region of the Zeeman slower. The slowed atoms are captured by the blue MOT beams operating on the 461 nm transition and trapped with the magnetic field generated by the magnetic coils arranged in the anti-Helmholtz configuration. Temperatures as low as 2 mK are achieved by this stage. Once the blue MOT beams are turned off, the red MOT beams operating on the 689 nm intercombination line further cool atoms to a few μK. Absorption imaging is used to determine the number and temperature of atoms in both MOTs. As will be seen in the next section, a PA laser resonantly excites colliding pairs of atoms from the red MOT into bound molecular states.

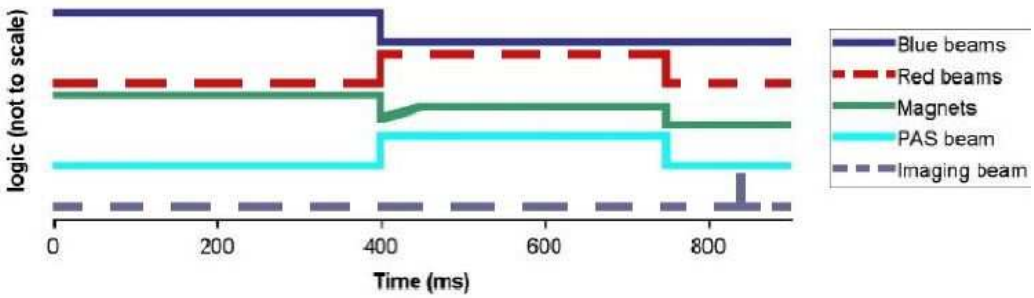

Figure 2.3 : The relative timing of events in the experiment is shown. The red MOT beams are turned on as the blue beams are shut off. The frequency of the red beams and the strength of the magnetic field are both ramped to different values in an effort to capture as many atoms from the blue MOT as possible. The PA beam may also be on during this time and is controlled by an acousto-optic modulator. The amount of time after the MOT and PA beams are turned off, but before the imaging beam is turned on, is adjustable.

to 800 μW/cm^2, are retroreflected. The intercombination line, at 7.5 kHz wide, is much more narrow than the 461 nm transition with a width of 32 MHz. Because the linewidth is so narrow, the Doppler temperature, which is usually the lower limit of cooling in other atoms, is very small (about 180 nK). In fact, for the intercombination line, the photon recoil temperature of about 460 nK is larger than the Doppler limit. All this means that atoms can be cooled much further than in the blue MOT, but because of the narrow line, the laser must first be artificially broadened so that a greater number of atoms can be transferred to the red MOT. As such, the red beams are detuned by about -1.3 MHz and experience a sine-wave modulation of 1.0 MHz. Figure 2.3 displays the relative timing of the experimental sequence of events.

During a 50 ms capture and equilibrium phase, the field gradient and the spectral

modulation are ramped up to 0.8 G/cm from 0.1 G/cm and down to ±0.7 MHz from ±1.0 MHz, respectively. This procedure results in 40 million ^{86}Sr atoms or 150 million ^{88}Sr atoms at temperatures of 5 and 8 μK, respectively. With no external influence, the lifetime of atoms in the red MOT is about 500 ms, and is limited by collisions with background gas in the vacuum apparatus. All told, the narrow width of the intercombination line transition has allowed one to cool the atoms several orders of magnitude below the temperature possible in the blue MOT and to hold them there for their lifetime.

Absorption imaging, a standard technique in atomic physics, is used to obtain parameters characterizing both MOTs: the number of atoms, the size of the atom cloud, the peak density, and the temperature are all determined from the optical depth of the atom cloud via absorption imaging. Laser light from the imaging beam, which is nearly resonant with the ^{1}S$_0$-^{1}P$_1$, 461 nm transition, is scattered off of atoms as the beam propagates through the sample. The scattering reduces the light intensity as follows: $I(z) = I_0 e^{-OD(x,y)}$, where $OD(x,y)$ is the afore-mentioned optical depth and the integral, along z, of the density distribution multiplied by the frequency-dependent absorption cross section, $\alpha(\nu)$:

$$OD(x,y) = \alpha(\nu) n_0^2 e^{-\frac{x^2}{2\sigma_x^2}} e^{-\frac{y^2}{2\sigma_y^2}} \int dz e^{-\frac{z^2}{2\sigma_z^2}}. \tag{2.1}$$

The OD is fit by a gaussian distribution to obtain the number of atoms, N, and the size of the cloud (σ) in two dimensions. The $1/\sqrt{e}$ radius of the cloud is 250 μm for ^{86}Sr and 400 μm for ^{88}Sr. The third dimension, along which the imaging occurs, is the axis parallel to gravity and perpendicular to the axial symmetry of the MOT. As the imaging reveals no information about the size in the vertical direction, another camera monitors fluorescence perpendicular to this direction. The size of the third dimension is smaller by approximately a factor of two in this axis, is estimated from

the sizes of the other two dimensions, and is one of the most important uncertainties in the experiment. Finally, using the number and the size yields an estimate for the peak density of the cloud, and its expression is

$$n_0 = \frac{N}{(2\pi)^{3/2}\sigma_x\sigma_y\sigma_z}. \tag{2.2}$$

The temperature is obtained by taking images a variable delay time after the MOT beams are turned off. The amount of expansion the cloud undergoes in a particular amount of time (t) in the ith dimension is a function of how hot (T) the atoms are:

$$\sigma_i^2 = \sigma_{i,0}^2 + \frac{2k_BT}{M} \times t^2, \tag{2.3}$$

where k_B is Boltzmann's constant and M is the reduced mass of an atom. The cloud size is plotted against this delay time, and a fit to the data yields the temperature of the atoms.

2.2 Photoassociation

Thus far, each of the experimental steps has been aimed at making the atoms cold enough to perform PAS. The final step involves using the photoassociation laser (PA laser) to perform the actual photoassociation experiment.

Once the red MOT is formed, there is an adjustable hold time ("interaction time") during which photoassociation is induced (again, see Fig. 2.3). This interaction time can be as long as the lifetime of the atoms in the red MOT (about 500 ms). A PA laser applied to the atoms during this hold time is tuned to the red of the atomic $^1S_0$ - $^1P_1$ transition at 461 nm. Second-harmonic generation in a linear enhancement cavity [29] produces the PA laser light. The cavity is seeded by light from an extended cavity diode laser at 922 nm. The linewidth of the laser is about 80 MHz in the blue,

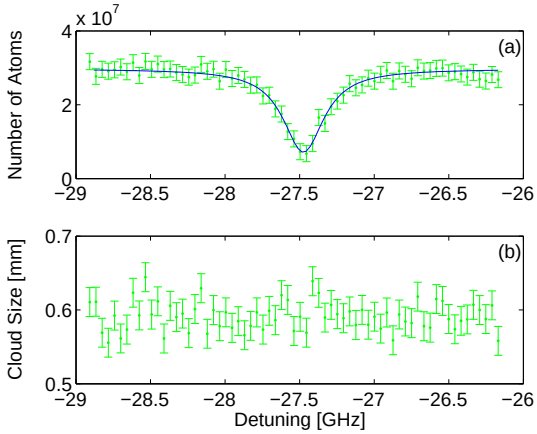

Figure 2.4 : (a) A typical photoassociation spectrum. The number of atoms is plotted against the laser frequency (GHz), shown as a detuning away from the principal resonance at 461 nm. The PA laser has little effect at the edges, away from the particular transition being probed. This means one can determine the red MOT's one-body loss rate without turning the PA laser off and possibly changing other MOT properties. (b) A systematic check of the system. The size of the atom cloud (in mm and measured 30 ms after the red MOT beams are turned off) is plotted versus the same laser detuning as for panel (a). Since the size of the atom cloud after 30 ms is an indication of its temperature, this graph indicates that the temperature of the cloud remains constant as the PA laser's frequency changes.

which is on the order of the natural linewidth of photoassociative transitions, γ_v ($\gamma_v \approx 2\Gamma$, where Γ is the natural linewidth of the principal atomic transition). The laser's frequency is measured using a wavemeter calibrated to the atomic $^1S_0$ - $^1P_1$ transition. The laser can have a power as high as 20 mW, and is used in several different configurations: typically, the beam is retroreflected and has a $1/e^2$ intensity radius of $w = 1$ mm. The maximum intensity the atoms see in this configuration is 3 W/cm^2, but as lower intensities are often necessary, an acousto-optic modulator is in place. In addition, there is sometimes a quarter-wave plate after the first path of the retroreflected beam so that the formation of a standing wave is avoided.

The PA laser excites photoassociative transitions between the atomic ground state and the excited molecular state potentials. When it is tuned across one of these transitions, the number of the atoms in the red MOT decreases because the photoassociation serves as an additional loss mechanism. Figure 2.4(a) shows data from a photoassociation spectrum of ^{86}Sr centered around a frequency 27.5 GHz red-detuned from the principal atomic resonance at 461 nm. Far enough from the molecular transition, the number of atoms for this particular transition appears to lie at some background level of about 30 million atoms. This number is different from the 40 million atoms quoted in the previous section because the finite lifetime of the atoms in the red MOT, due to one-body losses, means that, whether the PA laser is on or off, atoms will be lost from the trap during the interaction time. The uncertainty in the number of atoms is determined by sampling data points that are in the off-resonance, or background, portion of the spectrum. In the case of this data, the scan is well-centered, but other scans are less symmetric about the molecular transition, so the eight points furthest away from the transition are used to determine the statistical error in the number of atoms.

The observed photoassociation spectrum is uncomplicated for several reasons. The first is that, as mentioned earlier in Sec. 1.2, the bosonic isotopes of strontium lack hyperfine structure. The second is that the temperature of atoms in the red MOT is such that only s-wave collisions occur, meaning only $J = 1$ levels are excited. There are no higher rotational states to complicate the spectrum. Finally, of four states converging to the $^1S_0 + {}^1P_1$ asymptote, only the $^1\Sigma_u^+$ is excited in our experiment (recall Fig. 1.1). Two of the potentials contain no bound levels, and the other is inaccessible on the basis of selection rules.

It is important that other red MOT properties remain constant whether or not the PA laser is on-resonance. One such systematic check is to examine the size of the

atom cloud after a 30 ms delay between the time the red MOT and PA beams are turned off and the time that an image of the atoms is taken. Recall that absorption imaging only extracts information about the size of two dimensions. In this instance, it is not sufficiently accurate to estimate the size of the third dimension from the other two. A second camera is positioned to monitor the fluorescence in the direction perpendicular to that of the imaging beam. This monitor shows that, along this axis, the atom cloud is smaller by about a factor of two, thus allowing a better estimate of the total cloud volume. Figure 2.4(b) shows the cloud size after the 30 ms delay: it appears that the cloud size is constant with respect to the changing detuning of the PA laser, at least within the precision with which the size can be determined. The root-mean-square deviation describing the distribution of the measured cloud sizes is 0.02 mm, about 3% of the total cloud size. The constant size is good since the size of the cloud after the delay time correlates with the temperature of the atoms in the red MOT. The temperature should not change whether the PA laser is on- or off-resonance.

Because the rate at which atoms photoassociate is characterized by their loss from the trap, another systematic check must determine how having the PA laser on affects the loss rate. A rate equation is used to describe the change in the density of atoms over the time that the PA laser is applied to the atom cloud. The time-varying density is expressed as

$$\dot{n} = -\Gamma n - \beta' n^2 = -\Gamma n - \beta I n^2, \tag{2.4}$$

where Γ and β' are the one- and two-body loss rates, respectively, and β is the two-body decay rate for light with an intensity of 1 mW/cm^2. In this thesis, the intensity, I, will always be expressed in units of 1 mW/cm^2. One-body losses are thought to be attributable only to background gas collisions, while, as will be seen shortly,

two-body losses are due mainly to photoassociation, making β a good measure of the phenomenon. As will be discussed in the following chapter, the linear proportionality between β and the intensity is a good assumption for most of the data taken because the intensity is low and saturation effects are small. The laser beam waist is also 1.25 and 2 times bigger than the atom cloud for ^{88}Sr and ^{86}Sr, respectively. The sizes are compared by estimating the $1/e^2$ radii for both the atom cloud and the laser beam, with waist size, w. The overlap factor, $\zeta = w^2/(2\sigma^2 + w^2)$, between the laser and the atom cloud is not very different from unity. Effects on ζ due to non-linearities in the relationship between β and I will be the subject of future studies. The intensity of the laser, $I = I_0 e^{-\frac{2r^2}{w^2}}$, is of gaussian form, with I_0 being the peak intensity. Forming the integral leads to

$$\frac{dN}{dt} = -\Gamma n_0 \int d^3r e^{-\frac{r^2}{2\sigma^2}} - \beta n_0^2 I_0 \int d^3r e^{-\frac{2r^2}{w^2}} e^{-\frac{r^2}{\sigma^2}}. \tag{2.5}$$

Here, n_0 is the peak density and σ is the $1/\sqrt{e}$ radius of the atom cloud. The integrals represent the volumes in which one- and two-body interactions occur: different effective volumes describe each process. While the expressions for these volumes are helpful in solving the integral, how the volumes are defined is not central to this derivation. Therefore, their derivation has been relegated to Appendix A. Integration leads to the following differential equation:

$$\frac{dN}{dt} = -\Gamma N - \frac{\beta I_0 \zeta}{(2\sqrt{2\pi}\sigma)^3} N^2. \tag{2.6}$$

The term in the denominator results from the effective volumes, and ζ, as described above, accounts for the imperfect overlap between the PA laser and the atoms. Solving the differential equation yields an expression for the number of atoms as a function of time which contains both the one- and two-body loss rates and the peak number

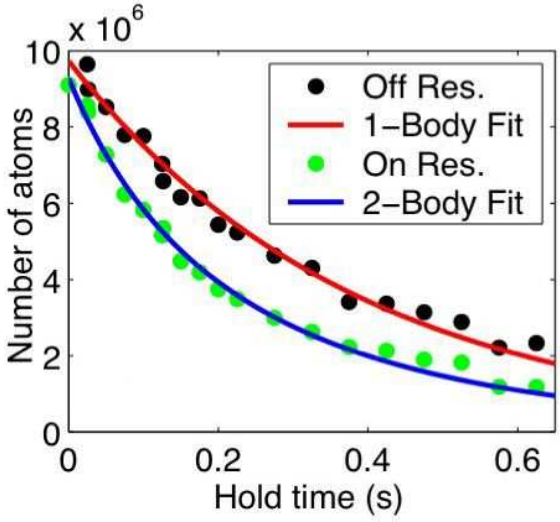

Figure 2.5 : The number of atoms in the red MOT is plotted as a function of the hold time. In both the on- and off-resonance cases, the PA laser is on. The off-resonance curve determines the value of Γ used to fit the on-resonance decay curve with Eq. 2.7. Taken from [27].

of atoms, N_0:

$$N(t) = \frac{N_0 e^{-\Gamma t}}{1 + \frac{N_0 \beta I_0 \zeta}{\Gamma(\sqrt{4\pi}\sigma)^3}(1 - e^{-\Gamma t})}. \tag{2.7}$$

The size, σ, is not a fit parameter. It is determined from images of the atom cloud, and it is measured with only a 1 ms delay prior to imaging the atoms (as compared to a 30 ms delay in the discussion of systematics, Fig. 2.4(b)). At 1 ms after the red MOT is turned off, the atoms have not had sufficient expansion time to change in size. The initial size of the cloud is taken to be $\sigma = (\sigma_x \sigma_y \sigma_z)^{1/3}$. The x and y sizes are easily obtained from the absorption image. The z size, as mentioned earlier, is about a factor of two smaller than the other dimensions, and it is estimated as $\sigma_z = \sqrt{\sigma_x \sigma_y}/2$.

Both the laser-atom overlap and the cloud size present measurement difficulties

which introduce systematic errors. The laser-atom overlap factor, ζ, attempts to quantify how well the PA beam is aligned to the atom cloud. Also, while the size of the atom cloud is periodically measured during the course of the experiment, measurements of the MOT indicate that the cloud size is somewhat dependent on intensity. The resulting increase in the cloud size is probably due to heating of atoms by off-resonant light scattering on the atomic transition. These two effects lead to a systematic uncertainty for the fitted value of β of about a factor of two.

The one-body decay rate, Γ, is also not a fit parameter. It is determined by an independent measurement. This is done because in measurements of the photoassociation rate, there is only a small deviation from the single exponential decay expected without photoassociation and because β and Γ are highly correlated (see Fig. 2.5). Fortunately, there is a straight-forward method to obtain Γ. From Eq. 2.7, it is clear that when there are no two-body losses ($\beta = 0$), $N(t)$ is only a single exponential decay. When the PA laser is off-resonance, β is small (as in the wings of Fig. 2.4(a)) and can be neglected given the accuracy of our measurements. Because all other processes remain the same, this means that the off-resonant decay curve yields a value of Γ obtained from a fit to the off-resonance curve. Γ is then fixed when fitting the on-resonance data. This data also demonstrates the model outlined by Eq. 2.7. During typical experimental runs, off-resonance lifetime measurements ($N(t)$) are taken occasionally, yielding periodic checks of Γ. This value of Γ is a constant when Eq. 2.7 is used to fit spectra as in Fig. 2.4.

Spectra such as Fig. 2.7, which yield most of the data, are usually taken for a single interaction time, and the time-dependence of the model is assumed. Therefore, it is possible that β is systematically varying in time. To check that this is not the case without the detailed study of Fig. 2.5, one would ideally have data for one transition at multiple interaction times. If the model held true, a plot of β versus

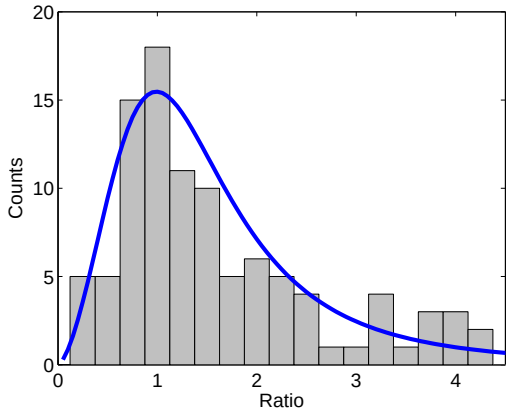

Figure 2.6 : A histogram of all the data points in the interaction time study. The horizontal axis is the ratio of the experimental to the theoretical collision rate. It is necessary to create the histogram in order to determine what distribution function best describes the distribution of the values of the ratio. Outliers in the data show up asymmetrically because a factor of two error in the ratio has a larger effect in the positive direction than in the negative direction. The log-logistic distribution was chosen because it best seems to describe the location of the peak of the data.

the interaction time would show no systematic variation of the photoassociation rate.

Unfortunately, there is too little experimental data for any particular transition studied to construct this ideal study. To increase the amount of data, the experimental β for a series of spectra taken under similar conditions is normalized by dividing by the theoretical rate for that transition. As will be seen in the next chapter, the theory is a good fit of the data in this set. This ratio should equal unity, but the systematic errors in the experiment, which may be a factor of two or three, further complicate the issue because outliers exist in the distribution of values. The ratio cannot be less than zero, however, leading to an asymmetry: that is, an experimental β twice as large as the theoretical rate is further from unity than an experimental β half as large as the theoretical rate. Figure 2.6 shows a histogram of all the in-

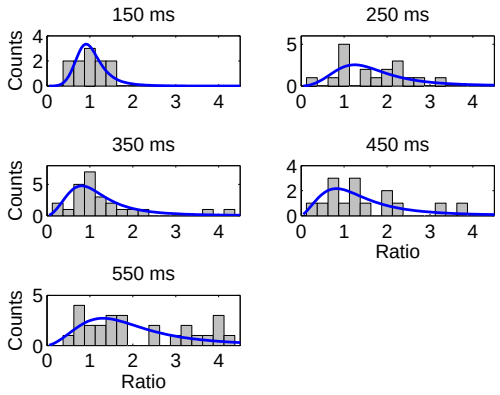

Figure 2.7 : The distribution of the ratio of the experimental to the theoretical two-body decay rate separated by interaction time. Each subplot contains only the data points from that interaction time. The distributions are histogrammed and fit with the log-logistic distribution, as in Fig. 2.6, to obtain the best value of the ratio of the experimental to the theoretical rate.

teraction times studied. The function used to fit the distribution, the log-logistic function, is chosen because the position of its peak value accurately characterizes the value of the ratio, and it fits this distribution well. A log-logistical distribution results if the logarithm of a variable is distributed according to the logistical distribution [30]. No attempt is made to justify the choice of this distribution beyond its phenomenological utility.

Applying this same fitting procedure to the rate data for each interaction time yields Fig. 2.7, which shows the individual distribution of ratios and the corresponding fits. The position of the peak of the fitting function in each subplot is the best value of the ratio. Fig. 2.8 shows those positions plotted against the interaction time. The exact position is determined by finding the zero value of the derivative of the distribution function. The error bars reflect the uncertainty in the parameters

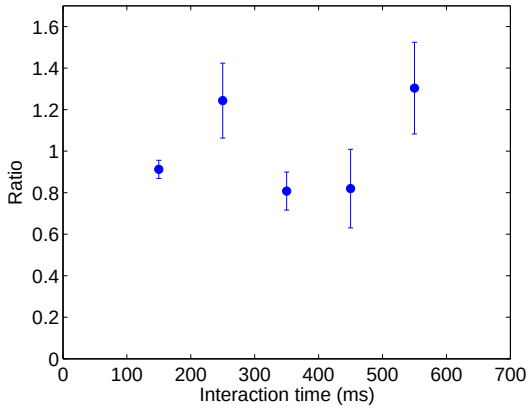

Figure 2.8 : The ratio of the experimental to the theoretical photoassociation rate plotted versus interaction time. The best value is determined by taking the derivative of the distributions appearing in Fig. 2.7, and the uncertainty in the peak value is determined by propagation of the error in the distribution parameters. With the model used, β should not vary with interaction time. Fortunately, there appears to be no systematic effect on the rate as a function of the time that the PA laser is on the atoms.

describing the distribution; they are found via propagation of error in the derivative. Upon examination, there is effectively no systematic trend of the ratio with respect to the interaction time. This conclusion is consistent with the model used to describe photoassociation.

In this chapter, I have discussed the experimental aspects of collecting photoassociation data and some of the systematic checks that have been done to double-check our assumptions. The data that results from these procedures is the foundation for the analysis that appears in the following chapter.

Chapter 3

Fitting and Analysis

This chapter, on the fitting and analysis of the photoassociation data, forms the core of my thesis. In it, I will review what the PAS data look like, how data are fit to extract parameters characterizing the system, how data compare with theoretical calculations, and how the systematics indicate behavior that requires correction during analysis. Henceforth, all discussion will be about ^{86}Sr because the new results that this thesis presents are for this isotope. The saturation behavior that is observed, and which requires correcting the two-body loss rate, occurs because the PA laser intensity was a significant fraction of the saturation intensity for some of the observed photoassociative transitions.

3.1 Deriving the Collision Rate

As I discussed in the previous chapter, the fundamental signature of photoassociation to look for during the experiment is a loss of atoms from the red MOT. Figure 2.4(a) shows data from a typical photoassociation spectrum; as the PA laser sweeps through the molecular transition, the number of atoms drops by more than 50%, indicating that it is, on a purely qualitative level, affecting the atom cloud in a manner that is consistent with expectations.

The two-body loss rate extracted from the fit in Fig. 2.4(a), β, characterizes this photoassociation signal. Because there are two atoms involved in each collision, the

two-body loss rate introduced in Eq. 2.4 is simply twice the collision rate constant, K. I use K in the remainder of my analysis because it is more commonly quoted in theoretical discussions of cold collisions. For atoms at very low temperatures and for an ideal PA laser (that is with linewidth narrower than the natural linewidth) at frequency, f, exciting a photoassociative transition with a center frequency, ν, the expression for the collision rate [31] is

$$K_v(T, I, f) = \frac{1}{hQ_T} \int_0^\infty d\epsilon e^{-\epsilon/k_B T} \frac{\gamma_v \gamma_s}{\{[\frac{\epsilon}{h} - (\nu - f)]^2 + (\frac{\gamma_v + \gamma_s}{2})^2\}}, \tag{3.1}$$

where $Q_T = (2\pi\mu k_B T/h^2)^{3/2}$, k_B is the Boltzmann constant, h is Planck's constant, μ is the reduced mass of strontium, ϵ is the kinetic energy of the initial state in question, and T is the temperature of the atoms in the red MOT. γ_v is the natural linewidth of the photoassociative transition, which is expected to be twice the value of the $^1P_1$ atomic decay rate $\tau_{^1P_1}^{-1} = 2\pi \times 30.5 s^{-1}$ [27]. Finally, $\gamma_s \equiv \gamma_s(\epsilon, J = 0)$ is the laser-stimulated width for the transition. One can use Fermi's golden rule to express this as $\gamma_s(\epsilon, J = 0) = \pi I d^2/\epsilon_0 c$ [32] as long as laser intensities are low enough to generate electric fields small compared to the Coulomb field of the atom. Here, ϵ_0 is the vacuum permittivity and c is the vacuum speed of light. $d^2 = |\langle v|D(R)|\epsilon\rangle|^2$ is the dipole matrix transition element. $D(R)$ connects the excited vibrational wave function, $|v\rangle$, and the energy normalized ground continuum wave function, $|\epsilon\rangle$. This treatment neglects light-induced shifts of levels [16], which are not observed and are not important to this analysis.

To determine the energy-dependence exactly, one needs to do a detailed calculation of the dipole matrix element connecting the ground state wave function to the excited state wave function. The underlying character of these wave functions predicts the variation in d^2 with energy. Jones et al. show in [33], however, that for some instances of low-energy scattering, intimate knowledge of the ground state

potential in the region where photoassociation occurs is not required to find the line shape. In these cases, the ground state wave function's amplitude scales as $\epsilon^{1/4}$, for J=0 angular momentum, while the energy does not affect its overall shape. This result is motivated by Wigner's observation [34] that some collisional properties at low energies are independent of the form of the short range potential and rely only on the angular momentum. As such, γ_s and d^2 will scale with the energy as $\epsilon^{1/2}$.

Reference [33] gives the following criterion for being in the Wigner threshold regime:

$$\frac{h\epsilon}{k_b} \ll \frac{\hbar^2}{2k_B h\mu R_0^2}\frac{2}{(0.6 - a_0/R_0)^2} \tag{3.2}$$

Here, $R_0 = \frac{2\mu C_6}{\hbar^2}$, μ is the reduced mass, C_6 is the coefficient in the C_n/R^n relation describing the ground state potential at long range, and a_0 is the scattering length in Bohr radii. I will discuss the scattering length of strontium in greater detail shortly. For the moment, however, it will suffice to say that for ^{86}Sr, assuming an energy on the order of k_BT, a scattering length about equal to $1000a_0$, and solving for T, one gets a threshold temperature of about 5 μK. This temperature is about equal to the temperature of atoms in the red MOT, meaning the Wigner law probably breaks down. Nevertheless, as a first approximation, its use is justified as follows. Figure 11 of [33] compares two scattering wave functions, one for a relatively small scattering length, which obeys the Wigner criterion, and the other for a larger scattering length. The latter wave function matches the former except at longer range where its curvature causes it to deviate from the Wigner law scaling. The authors of this paper state that where disagreement with the threshold law begins is dependent on the particular distances for the photoassociative transition being studied. The induced error from assuming the Wigner regime is expected to be small, but the next step in the analysis, which is beyond the scope of this thesis, will be solving for the

exact energy-dependence of the dipole matrix elements.

The energy dependence of $\gamma_s(\epsilon, J = 0)$ in the Wigner law regime takes the functional form of $AI\epsilon^{1/2}$ [31], where A is a constant pre-factor. Because of the energy-dependence of γ_s and the presence of an energy term in the denominator of Eq. 3.1, analytically evaluating Eq. 3.1 is not possible to the best of our knowledge. As a simplification, I show, by comparison with the numerically-calculated integral, that the integrand evaluated at about k_BT may replace the integral for sufficiently low energies (see Appendix B). With this substitution and some algebraic manipulation, the expression for the collision rate becomes

$$K_v(T, I, f) = \frac{k_BT}{hQ_T} \frac{4\gamma_v\gamma_s(\epsilon', I)}{[\gamma_v + \gamma_s(\epsilon', I)]^2} \frac{1}{1 + \frac{4[\frac{\epsilon'}{h} - (\nu - f)]^2}{[\gamma_v + \gamma_s(\epsilon', I)]^2}}, \tag{3.3}$$

with $\gamma_s(I) = AI\epsilon'^{1/2}$. As discussed in Appendix B, $\epsilon' = xk_BT$ is approximately equal to k_BT; the exact proportion is determined from fitting the numerically-calculated Eq. 3.1. $x = 0.78$ for $I << I_{sat}$, and it decreases to $x = 0.50$ as I/I_{sat} approaches unity. The ϵ'/h term will have the largest effect at resonance ($\nu = f$). In that instance, if $\frac{4(\frac{\epsilon'}{h})^2}{[\gamma_v + \gamma_s(I)]^2}$ is much less than unity, then the ϵ'/h part of this expression can safely be neglected for all frequencies. For an energy about equal to k_BT and a temperature of 5 μK, the value of the expression is on the order of 10^{-5} which is, indeed, much smaller than unity. In contrast, the condition certainly does not hold true for a typical blue MOT temperature of 2 mK because the expression is then on the order of unity. As the red MOT is at 5 μK, the expression for the collision rate can be rewritten such that the portion not containing the frequency dependence is the on-resonance collision rate. That is,

$$K_v(T, I, f) = K_v^{res}(T, I) \frac{1}{1 + \frac{4(\nu - f)^2}{[\gamma_v + \gamma_s(I)]^2}}, \tag{3.4}$$

where

$$K_v^{res}(T,I) = \frac{k_B T}{hQ_T}\frac{4\gamma_v\gamma_s(I)}{[\gamma_v+\gamma_s(I)]^2}. \tag{3.5}$$

The on-resonant collision rate is often quoted for an intensity of 1 mW/cm^2. To reflect this, one additional modification is made to this expression by introducing the collision rate for 1 mW/cm^2 light:

$$K_v(T,I,f) = K_v^{res}(T,1\mathrm{mW/cm^2})\frac{K_v^{res}(T,I)}{K_v^{res}(T,1\mathrm{mW/cm^2})}\frac{1}{1+\frac{4(\nu-f)^2}{[\gamma_v+\gamma_s(I)]^2}}. \tag{3.6}$$

From now on, I will label the ratio, $\frac{K_v^{res}(T,I)}{K_v^{res}(T,1mW/cm^2)}$, as $K_{ratio}(I)$. The probability of photoassociation is the same for all pairs of atoms, and so the interaction of atoms is expected to produce homogeneous broadening [35]. $\gamma_v+\gamma_s$ can be interpreted as the rate at which molecules leave the excited state, and the line shape of this decay is expected to be Lorentzian since the molecule behaves like a damped oscillator. Because the linewidth of the PA laser (about 90 MHz) is on the order of the natural linewidth (61 MHz), it cannot be neglected in this analysis. A phenomenological Lorentzian is used to represent the line shape of the laser and any additional broadening that may occur [17, 18], and it results in the following convolution of two Lorentzian line shapes:

$$K_v^{exp}(T,I) = K_v^{res}(T,1\mathrm{mW/cm^2})K_{ratio}(I)\times \int df\frac{1}{\pi}\frac{\gamma_{phen}/2}{(\gamma_{phen}/2)^2+(f-f_{laser})^2}\times\frac{1}{1+\frac{4(f-\nu)^2}{[\gamma_v+\gamma_s(I)]^2}}. \tag{3.7}$$

Here, f_{laser} is the center frequency of the laser. γ_{phen} is usually the linewidth of the laser, but may include, for example, additional line-broadening effects that are seen at large detuning for ^{86}Sr. The result of the convolution is

$$K_v^{exp}(T,I) = K_v^{res}(T,1\mathrm{mW/cm^2})K_{ratio}(I)\frac{\gamma_v+\gamma_s(I)}{\gamma_{phen}+\gamma_v+\gamma_s(I)}\frac{1}{1+\frac{4(v-f_{laser})^2}{[\gamma_{phen}+\gamma_v+\gamma_s(I)]^2}}, \tag{3.8}$$

which contains the sum of the linewidths and the detuning between the laser's center frequency and the resonance frequency. A key point is that the convolution preserves the integrated area of the transition. This analysis could have been done in a way that was independent of a model for the laser linewidth by working with spectral-line integrated areas, and the results would have been the same. The total linewidth, $\gamma = \gamma_{phen} + \gamma_v + \gamma_s(I)$, is the experimentally-observed linewidth. K_{ratio} is found from theory that is a very good fit of the data [1]. This is a little circular, but the function that describes the data is valid only for an intensity of 1 mW/cm^2. As will be discussed in Section 3.2, some transitions are subject to higher intensities and K_{ratio} allows normalization to the rate for 1 mW/cm^2. The actual fitting routine uses Eq. 2.7 to produce the fit curve seen in Fig. 2.4(a). β, in Eq. 2.7, takes the form of Eq. 3.8, with the appropriate conversion between the collision rate and the two-body loss rate.

Fitting each molecular transition in this manner and detuning the center frequency of the laser by up to 1400 GHz red of the atomic resonance in order to detect different transitions, yields the full photoassociation spectrum (Fig. 3.1). Figure 3.2 plots the resonant collision rate at 1 mW/cm^2 intensity, $K_v^{res}(T, 1\text{mW/cm}^2)$, against the laser detuning. The reason the data is normalized to 1 mW/cm^2 laser light is for comparison with theory. Not all the data was taken under identical experimental conditions, and the symbols on the plot reflect the intensities that were used to probe each molecular transition.

Robin Côté and Philippe Pellegrini at the University of Connecticut performed the analysis leading to the theory curve displayed in Fig. 3.2. This analysis determines the wave functions using a full quantum calculation to evaluate Eq. 3.1 theoretically. γ_v and d are found from the overlap integral between the colliding state, $|\epsilon\rangle$, and the excited state, $|\nu\rangle$. The potentials are formed by joining various

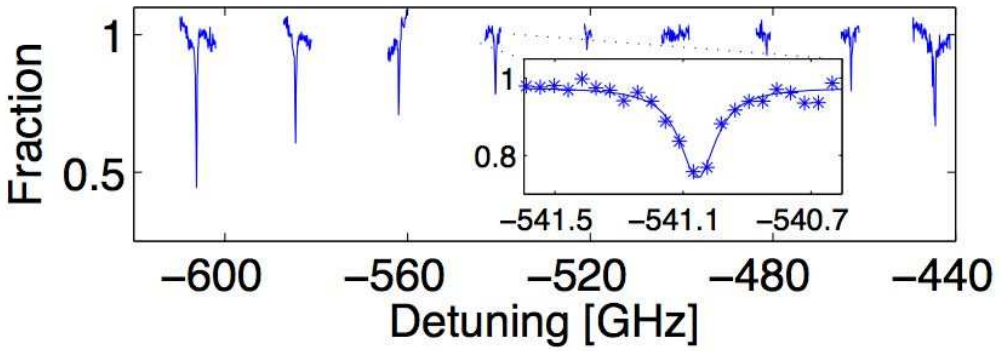

Figure 3.1 : A portion of the photoassociation spectrum. Each of the resonances corresponds to a different molecular transition. The strength of the lines (amplitude) varies by transition. The spectrum containing all of the observed transitions stretches from a few GHz red-detuned to -1300 GHz. As will be seen, the minimum that appears near -500 GHz helps theorists determine the scattering length of ^{86}Sr. The inset shows data similar to that found in Fig. 2.4. Taken from [1].

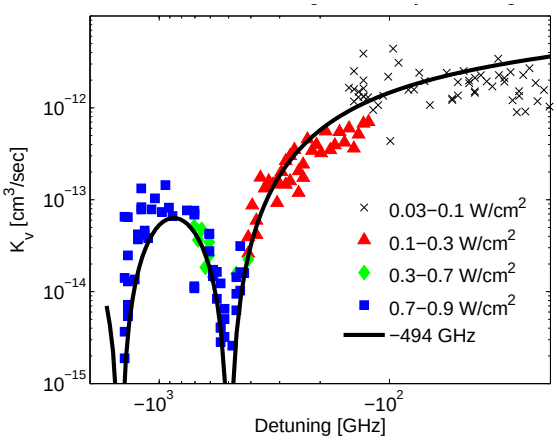

Figure 3.2 : Experimental collision rates for ^{86}Sr have been calculated from intensity-dependent two-body loss rates and normalized to 1 mW/cm^2 for comparison with theory. The spectrum of molecular transitions is shown as a function of the laser detuning from the atomic resonance at 461 nm. As discussed in Section 3.2, the data is corrected for saturation at the unitarity limit, and it has its largest effect at small detunings.

short and long range forms. The inner parts of the ground and excited state potentials use an experimental Rydberg-Klein-Rees potential from [36] and an *ab initio* potential from [37], respectively. The longer range potential in either case is of the form C_n/R^n, which apply for larger separation of the colliding atoms. Only the C_3 coefficient is necessary for the excited state potential, while the C_6 coefficient contributes to the ground state potential. The wave functions are found via a full quantum calculation using the molecular potentials.

The transition rates vary according to the amount of overlap in the ground and excited state wave functions. The minimum rate of the data shown in Fig. 3.2 corresponds to a node in the ground state wave function. To pin down the frequency (detuning) at which the photoassociation rate goes to zero, multiple possible potential curves are generated by varying the position of the repulsive inner wall. While the C_6 coefficient used to characterize the ground state potential affects the overall fit to the data, the position of the experimental minimum itself varies little for different values of C_6. The theorists can determine the position of the node in the ground state wave function using the location of the minimum. Therefore, the position of the experimental minimum and C_6 determine the potential that describes the collisional properties of the system.

The potential curve that best fits the data by a least squares fit is the theory curve displayed in Fig. 3.2. From it, one can figure out the s-wave scattering length from the calculated ground state wave function. The scattering length effectively summarizes the collisional properties of the system. The published values of C_6 vary considerably, however, and make it difficult to assign a best value for the scattering length. Therefore, bounds on the scattering length, a_{86}, are determined using several quoted values of C_6 [1] and one standard deviation variation in the node position, resulting in a quoted range for the scattering length of $610a_0 < a_{86} < 2300a_0$.

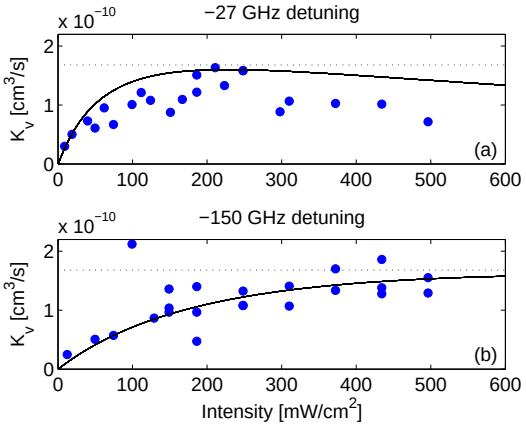

Figure 3.3 : (a) Saturation of the collision rate is observed in this plot of the collision rate as a function of intensity for -27 GHz detuning from the atomic resonance. The intensity at which saturation occurs is transition-dependent, but the maximum such rate for 5 μK atoms is represented by the dotted line in the figure. Saturation does not occur until $\gamma_v \approx \gamma_s(I)$. (b) The same effect is observed for a -150 GHz detuning from the atomic resonance.

This analysis, for both isotopes of strontium, is described in a paper [1] recently published in *Physical Review Letters*. This thesis is not about the fitting procedure just described; the intensity studies are an addition to the previous study.

3.2 Intensity Studies

Intensity studies of the photoassociation process are particularly important because they enhance one's understanding of the physical processes at work. Examination of the collision rate as a function of intensity reveals saturation behavior that is attributable to the quantum mechanical unitarity limit. In this section, I present the data that suggests this behavior occurs and discuss how the full Eq. 3.1 is used to account for saturation effects.

The effect of high intensity laser light on the photoassociation signal is most

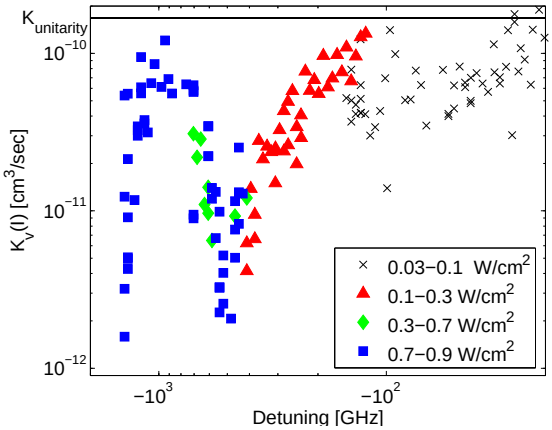

Figure 3.4 : $K_v(T, I)$ is plotted against detuning from the atomic transition. The solid line at about 2x10^{-10} cm^3/s represents the maximum collision rate possible for 5 μK atoms. Molecular transitions probed with lower intensity laser light will likely not approach the unitarity limit as the saturation condition, $\gamma_v \approx \gamma_s(I)$, is not satisfied. Nevertheless, a number of data points do approach this maximum rate. It indicates that the saturation observed in Fig. 3.3 is likely due to the quantum mechanical unitarity limit.

clearly seen in Fig. 3.3. The intensity-dependent collision rate, K_v, from Eq. 3.8 is plotted against the intensity of the PA laser for two different laser detunings, one at -27 GHz and one at -150 GHz from the atomic resonance. Qualitatively, it is clear that the relationship between the collision rate and the intensity is not linear. If the relationship were linear, then the derivation of the collision rate in Section 3.1 would be simplified because an intensity-dependent K_v would need not be calculated.

Why might this saturation behavior be occurring? The density of atoms in the red MOT is not high enough to expect collisional broadening, but if the intensity is equal to the saturation intensity of the molecular transition, then it is reasonable to expect the collision rate to peak. An estimate of the maximum value of the collision rate can be made using Eq. 3.4 [16]. The maximum occurs on-resonance and when

$\gamma_v = \gamma_s(I)$, resulting in the following expression for the maximum K:

$$K_{sat}(T, I_{sat}) = \frac{k_B T}{h Q_T} = \frac{h^2}{(2\pi\mu)^{3/2}} \frac{1}{\sqrt{k_B T}}. \tag{3.9}$$

This expression only depends on the temperature of the red MOT. For atoms at 5 μK, the maximum collision rate that any transition could have is calculated to be 1.68×10^{-10}cm^3/s. This limit is known as the quantum mechanical scattering limit, as it results from approaching the maximum scattering probability.

In practice, the unitarity limit for any particular molecular transition may not approach the maximum rate because the overlap between the ground and the excited states is small, making the transition weak. Also, experimentally, the intensity of the incident laser light is changed for each transition in order to maximize the photoassociation signal. While Figure 3.2, for the full spectrum of detuning, shows the variation of the rate by transition, it is normalized for I=1 mW/cm^2 light; one cannot determine whether the collision rate approaches the unitarity limit. Figure 3.4, in contrast, shows the intensity-dependent $K_v(I)$, and it makes sense to mark the maximum possible unitarity limit estimated from Eq. 3.9*. This plot suggests that a subset of the data is subject to saturation effects such as those seen in Fig. 3.3.

Another way to check for saturation is to look at the intensity as a fraction of the saturation intensity for each transition. Figure 3.5(a) shows the percentage of the saturation intensity achieved for each transition. A significant number of transitions are at 20% to 30% of saturation, and these same points appear to correspond with the points that approach the unitarity limit in Fig. 3.4. The data of Fig. 3.2 account for saturation via $K_{ratio}(I)$. One's intuition for $K_{ratio}(I)$ is that for low intensities,

*The unitarity limit is marked in similar fashion for the plots of Fig. 3.3.

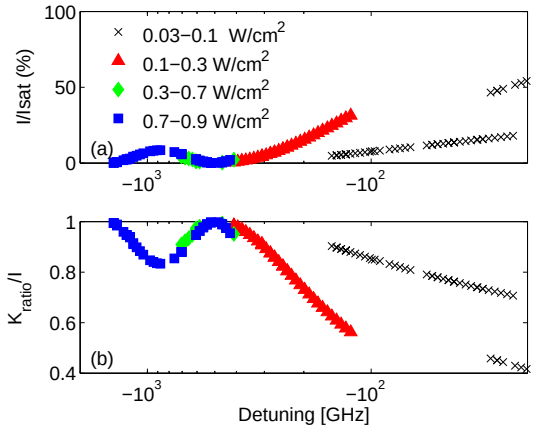

Figure 3.5 : (a) The percent of the saturation intensity used for each transition. Many of the transitions operate well-below the saturation intensity where a linear relation between K_v and the intensity is a good approximation. For other transitions, this is not the case, and the intensity-dependence is more complicated. K_{ratio}, of Eq. 3.7 accounts for non-linear intensity dependence in cases where the applied intensity is a large fraction of saturation. (b) K_{ratio} is divided by the laser intensity and also plotted against the detuning. Except where the intensity approaches saturation, this ratio is close to unity. This is the case because $K_v(I) \rightarrow K_v(1\ \mathrm{mW/cm^2})$ as the intensity approaches 1 mW/cm^2. Note that the legend from panel (a) also applies to panel (b).

it will scale linearly with intensity. Then, at intensities closer to I_{sat}, $K_{ratio}(I)$ will deviate more from the linear relationship. In Figure 3.5(b), K_{ratio} is divided by the intensity and plotted against the detuning. At intensities close to 1 mW/cm^2, K_{ratio} is equal to 1, and divided by I=1, the total ratio is about 1. In cases where the saturation intensity is reached, the deviation of the ratio from unity grows larger. Transitions that one expects to have saturate, namely ones closer to resonance, or ones with fairly large applied PA laser intensities, show some of the largest deviations from unity.

Applying the theory to a particular transition and calculating it for 5 μK atoms

results in the theory curves seen in Fig. 3.3. The -27 GHz detuning transition in particular, has some interesting features. Not only does the value of the collision rate saturate with increasing intensity, but it rolls over. That is, K_v reaches a maximum at I_{sat} and then starts decreasing despite the still-increasing intensity. For a normal bound-bound system, this behavior seems strange because one expects the collision rate to saturate by approaching the unitarity limit asymptotically. This is not the case here because one of the states is a scattering state instead of a bound state.

To understand the difference, one may think of the resonance as a Landau-Zener crossing [38, 39] as in Fig. 3.6. Panel (a) of the figure shows the uncoupled energy levels of a two level system and that they are degenerate at their crossing point. Panel (b) shows the avoided crossing resulting from the coupling of the two energy levels. The uncoupled degenerate energy levels are expressed in the coupled state basis with the dressed picture. As the atoms interact along the ground state potential and the electric field of the laser couples them with the bound molecular state, there is a chance of the photoassociative transition from one level to the other. The probability of making the transition is not unity, however, as the atoms may also approach each other even more closely along the ground state potential. As they collide, they re-separate and come into resonance one more time as they drift apart.

The size of the gap between the dressed energy levels depends on the intensity of the light. Examining this gap size may explain the roll-over effect seen in the intensity plots because the size of the gap affects the likelihood of a transition. For a small gap created by low intensity light, a transition is fairly likely to occur. However, if there is zero coupling, then there will be no transition at all. Similarly, at high intensity, the gap is larger and the likelihood of the transition is lower. Therefore, some optimum intensity corresponds to the maximum of the transition rate near the unitarity limit. In short, the intensity tunes the gap between the two states such that

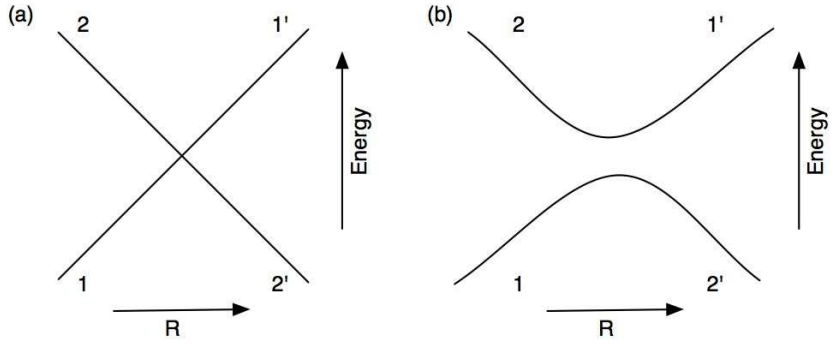

Figure 3.6 : The energy of levels in a two-level system. (a) With no coupling between the two states, they are degenerate. There is no chance of changing from state 1 to state $2'$ as the variable R changes in time (such as a collision). (b) In the dressed picture, the two states are coupled by the electric field of the laser. There is an avoided crossing according to the no-crossing theorem [40]. The probability of changing states depends on the size of the gap which, in turn, depends on the laser intensity. The relationship between the intensity and the transition rate may explain why roll-over is observed in the intensity studies.

I_{sat} corresponds to the point where a transition is most likely to occur. As far as we know [16, 18, 20], this behavior has not previously been observed in photoassociation experiments and is a new result.

In sum, the intensity studies I present here indicate that saturation due to the unitarity limit is a feature for a significant number of the observed molecular transitions. In addition, some of the data demonstrates roll-over of the collision rate, a phenomenon not previously observed in photoassociation. The same studies also indicate that a correct analysis of the data for all detunings involves accounting for the intensity in the calculation of collision rates. Without doubt, these intensity studies tease additional interesting physics from the photoassociation experiment.

Chapter 4

Conclusion

This thesis has demonstrated saturation of photoassociative molecular transitions at the quantum mechanical unitarity limit. This work also reveals some interesting features that occur at saturation and improves previous experiments on photoassociation that determined the scattering lengths of Sr. To date, not a lot of work has been done with high intensity light, particularly for group II elements like Sr, so this work points the way to relatively unexplored areas.

As mentioned in the introduction, three categories of information come from photoassociation experiments. Photoassociation line shapes can be examined for information about collisions, the absorption spectrum can be mapped out to gain insight on excited state potentials, and the intensity modulation of the absorption spectrum will reveal features of the ground state wave function. The photoassociation experiments [27, 1] that were previously performed in the Killian lab explored the latter two categories in some depth. The first experiment [27] studied the properties of the excited state potential at very long range. The second experiment [1] determined the scattering length of strontium, something gained from examining the ground state wave function. Finally, this work has studied the effects of saturation on the individual lines and allowed the refinement of data from previous experiments.

While these studies have observed interesting physics, they have only scratched the surface of what is possible. Many questions remain to be asked and answered, and many refinements will be worth pursuing. For instance, one can already see wanting

to determine the energy-dependence of dipole-matrix elements exactly to avoid problems associated with being outside the Wigner threshold regime. Additionally, line shape features are predicted by theorists [14] to appear at high intensities. These extra peaks and/or line shifts will reveal yet more information about collisional dynamics at ultracold temperatures. Nevertheless, effectively treating these systems theoretically is challenging, and further experiments may yield surprising results despite our best predictions.

Appendix A

Defining Effective Volumes

The characteristic volume in which one-body processes occur is different than that in which two-body or higher-body processes occur. In this appendix, I derive expressions for the one-body and two-body effective volumes which are used in Section 2.2.

I begin by defining the density, n as

$$n = n_0 e^{-\frac{r^m}{\rho^m}} = \frac{N}{V_{m,1}} e^{-\frac{r^m}{\rho^m}} \tag{A.1}$$

where N is the number of particles, r is the radial coordinate in a spherical coordinate system, ρ is a size characteristic of the cloud of atoms, and m is the exponent (usually 2). Note that $N = n_0 V_{m,1}$. Integrating the density over the volume yields

$$N = \int d^3 r n(r) = n_0 \int d^3 r e^{-\frac{r^m}{\rho^m}} = n_0 4\pi \int dr r^2 e^{-\frac{-r^m}{\rho^m}}. \tag{A.2}$$

Next, making the substitution $z = r/\rho$ results in

$$N = n_0 4\pi\rho^3 \int dz z^2 e^{-z^m} = n_0 4\pi\rho^3 \frac{1}{3}\Gamma[1 + \frac{3}{m}], \tag{A.3}$$

with Γ being the usual gamma function. The general case of the one-body volume is therefore,

$$V_{m,1} = 4\pi\rho^3 \frac{1}{3}\Gamma[1 + \frac{3}{m}]. \tag{A.4}$$

More specifically, in the case where m=2 and $\rho = \sqrt{2}\sigma$, the gamma function is equal to $3\sqrt{\pi}/4$ and $V_{2,1} = (\sqrt{2\pi}\sigma)^3$.

In the two-body case, I start with the time-dependent expression for the density, $\dot{n} = -\beta n^2$. Integrating over the volume, d^3r yields

$$\dot{N} = \int d^3r\dot{n} = -\beta n_0^2 \int d^3r e^{-2\frac{r^m}{\rho^m}}. \tag{A.5}$$

The integral represents $V_{m,2}$ and performing the substitution $z = 2^{1/m}r^m$ leads to

$$V_{m,2} = \int d^3r e^{-2\frac{r^m}{\rho^m}} = \frac{4\pi}{2^{3/m}} \int dz z^2 e^{-\frac{-r^m}{\rho^m}}, \tag{A.6}$$

which is simply the one-body volume from above. This implies that

$$V_{m,2} = \frac{V_{m,1}}{2^{3/m}} \tag{A.7}$$

Again inputting m=2 and $\rho = \sqrt{2}\sigma$, the two-body volume is $V_{2,2} = (\sqrt{\pi}\sigma)^3$.

Note that the two-body volume is smaller because it describes the fact that processes requiring collisions of two particles happen more often in higher density regions.

Appendix B

Approximating the Integral in Eq. 3.1

This appendix demonstrates that solving the integral in Eq. 3.1 by replacing the full integral with the integrand evaluated at $\epsilon = xk_BT$ is valid for cases where the applied light intensity is much less than the saturation intensity of the molecular transition. With the energy-dependence present in γ_s, the integral in Eq. 3.1 is difficult to approach analytically. Nevertheless, in the quest for an expression like Eq. 3.8 for the experimental collision rate, it is desirable to have a solution valid even if it is only applicable in a limited regime.

I will demonstrate that the integrand is an adequate replacement for the integral by comparing it to the numerically-calculated integral for a variety of conditions. Finding the integrand in unit-less form will simplify its calculation, so that is how I begin. The integrand initially looks like

$$\frac{4\gamma_\nu\gamma_s}{(\gamma_\nu+\gamma_s)^2+4(\frac{\epsilon'}{h}-f)^2}, \tag{B.1}$$

where $\epsilon' = xk_BT$ and x is an adjustable parameter. For the purposes of this demonstration, I have chosen the center of the lineshape to be at zero frequency. Substituting in the Wigner law expression for the stimulated linewidth yields,

$$\frac{4\gamma_\nu A_0 I\sqrt{\epsilon'}\frac{\sqrt{k_BT}}{\gamma_\nu^2\sqrt{k_BT}}}{(1+\frac{\sqrt{k_BT}}{\gamma_\nu^2\sqrt{k_BT}}A_0I\sqrt{\epsilon'})^2+\frac{4}{\gamma_\nu^2}(\frac{\epsilon'}{h}-f)^2}, \tag{B.2}$$

which looks complicated until I define the saturation intensity. Saturation of a transition occurs as the stimulated linewidth approaches the natural linewidth. Again

using the Wigner law expression for the stimulated linewidth and solving for the intensity assuming an energy k_BT,

$$I_s = \frac{\gamma_\nu}{A_0\sqrt{k_BT}}. \tag{B.3}$$

Now, I_s is substituted into Eq. B.2 and results in

$$\frac{4\frac{I}{I_s}\sqrt{\frac{\epsilon'}{k_BT}}}{(1+\frac{I}{I_s}\sqrt{\frac{\epsilon'}{k_BT}})^2+\frac{4}{\gamma_\nu^2}(\frac{\epsilon'}{h}-f)^2}. \tag{B.4}$$

The intensity can now neatly be expressed as a fraction of the saturation intensity.

What is really happening with this simplification is that the integrand is being evaluated at one value of the energy instead of, in the case of the integral, being evaluated at all possible energies. Because many of the energies in the distribution do not lead to large values of the integrand, it is possible to use an average value of the energy to approximate the full distribution. In this case, that average value is about equal to k_BT. x,, the exact fraction of k_BT, is determined by fitting the integrand to points from the numerically-calculated integral. Figure B.1 shows the fitted integrand for an intensity equal to one percent of the saturation intensity. In this case, $x = 0.78$, and the fit in this case is excellent.

What, then, is the maximum percentage of saturation that the intensity can take on before the approximation of the integrand to the integral breaks down? To answer this question, Fig. B.2 shows several data sets and fitted curves. From bottom to top, the intensities are $1\%I$, $10\%I$, $50\%I$, and $100\%I$. By the time the intensity is 50% of saturation, there are clear differences between the two cases. At saturation, if one were to use this approximation to fit the data, the peak rate would likely be overestimated, while the width of the line would be underestimated. The appropriate value of x for the laser intensity of any particular molecular transition is used during analysis.

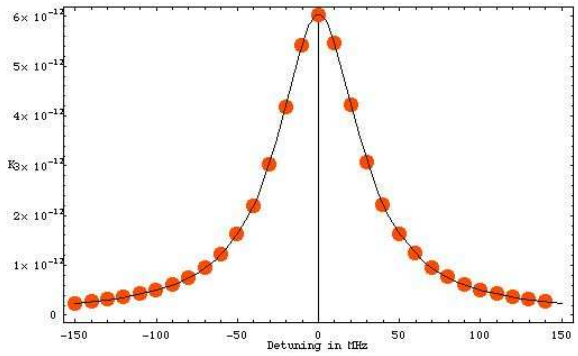

Figure B.1 : A comparison of the integral portion of the collision rate to the integrand of the integral. The collision rate contains an integral that is challenging to solve analytically. This plot compares the numerically-calculated integral (data points) to the fitted expression for the integrand which has one adjustable parameter: x, the fraction of $k_B T$ that is the value of the energy the integrand is evaluated at. This fit is for an intensity which is one percent of the saturation intensity.

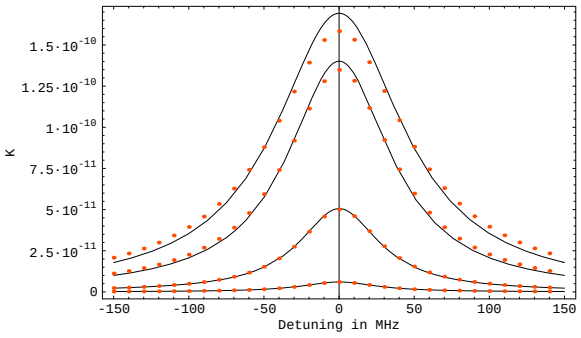

Figure B.2 : The same comparison as in Fig. B.1 made for different values of the intensity. From bottom to top, the intensity is 1%, 10%, 50%, and 100% of the saturation intensity. The approximation of the integrand to the integral breaks down as the intensity approaches the saturation intensity. For each of these fits, and again from bottom to top, x equals 0.78, 0.73, 0.60, and 0.51.

Bibliography

[1] P. Mickelson, Y. Martinez, A. Saenz, S. Nagel, Y. C. Chen, T. Killian, P. Pellegrini, R. Coté: *Physical Review Letters* **95**, 223002 (2005).

[2] H. J. Metcalf, P. van der Straten: *Laser Cooling and Trapping*: Graduate Texts in Contemporary Physics. Springer, New York (1999).

[3] T. W. Hänsch, A. L. Schawlow: *Optics Communications* **13**, 68 (1975).

[4] D. Wineland, H. Dehmelt: *Bulletin of the American Physical Society* **20**, 637 (1975).

[5] W. D. Phillips, H. J. Metcalf: *Physical Review Letters* **48**, 596 (1982).

[6] J. Prodan, A. Migdal, W. D. Phillips, I. So, H. J. Metcalf, J. Dalibard: *Physical Review Letters* **54**, 992 (1985).

[7] J. Dalibard, W. D. Phillips: *Bulletin of the American Physical Society* **30**, 748 (1985).

[8] S. Chu, L. Hollberg, J. Bjorkholm, A. Cable, A. Ashkin: *Physical Review Letters* **55**, 48 (1985).

[9] E. Raab, M. Prentiss, A. Cable, S. Chu, D. Pritchard: *Physical Review Letters* **59**, 2631 (1987).

[10] H. Thorsheim, J. Weiner, P. Julienne: *Physical Review Letters* **58**, 2420 (1987).

[11] H. Scheingraber, C. R. Vidal: *Journal of Chemical Physics* **66**, 3694 (1977).

[12] R. B. Jones, J. H. Schloss, J. G. Eden: *Journal of Chemical Physics* **98**, 4317 (1993).

[13] R. A. Cline, J. D. Miller, D. J. Heinzen: *Physical Review Letters* **73**, 632 (1993).

[14] A. Simoni, P. Julienne, E. Tiesinga, C. Williams: *Physical Review A* **66**, 063406 (2002).

[15] E. Ribeiro, A. Zanelatto, R. d. J. Napolitano: *Chemical Physics Letters* **390**, 89 (2004).

[16] I. D. Prodan, M. Pichler, M. Junker, R. G. Hulet, J. L. Bohn: *Physical Review Letters* **91**, 080402 (2003).

[17] C. McKenzie, J. H. Denschlag, H. Häffner, A. Browaeys, L. E. E. de Araujo, F. K. Fatemi, K. M. Jones, J. E. Simsarian, D. Cho, A. Simoni, E. Tiesinga, P. S. Julienne, K. Helmerson, P. D. Lett, S. L. Rolston, W. D. Phillips: *Physical Review Letters* **88**, 120403 (2002).

[18] U. Schlöder, C. Silber, T. Deuschle, C. Zimmermann: *Physical Review A* **66**, 061403(R) (2002).

[19] J. Ramirez-Serrano, W. DeGraffenreid, J. Weiner, E. Tiesinga, P. S. Julienne: *Physical Review A* **69**, 042708 (2004).

[20] S. Kraft, M. Mudrich, M. Staudt, J. Lange, O. Dulieu, R. Wester, M. Weidemüller: *Physical Review A* **71**, 013417 (2005).

[21] J. Weiner, V. S. Bagnato, S. Zilio, P. S. Julienne: *Reviews of Modern Physics* **71**, 1 (1999).

[22] M. Machholm, P. S. Julienne, K.-A. Suominen: *Physical Review A* **64**, 033425 (2001).

[23] S. B. Nagel, C. E. Simien, S. Laha, P. Gupta, V. S. Ashoka, T. C. Killian: *Physical Review A* **67**, 011401 (2003).

[24] H. Katori, T. Ido, Y. Isoya, M. Kuwata-Gonokami: *Physical Review Letters* **82**, 1116 (1999).

[25] G. Zinner, T. Binnewies, F. Riehle, E. Tiemann: *Physical Review Letters* **85**, 2292 (2000).

[26] C. Degenhardt, T. Binnewies, G. Wilpers, U. Sterr, F. Riehle, C. Lisdat, E. Tiemann: *Physical Review A* **67**, 043408 (2003).

[27] S. Nagel, P. Mickelson, A. Saenz, Y. Martinez, Y. Chen, T. Killian, P. Pellegrini, R. Côté: *Physical Review Letters* **94**, 083004 (2005).

[28] G. Ferrari, P. Cancio, R. Drullinger, G. Giusfredi, N. Poli, M. Prevedelli, C. Toninelli, G. M. Tino: *Physical Review Letters* **91**, 243002 (2003).

[29] M. Bode, I. Freitag, A. Tünnermann, H. Welling: *Optics Letters* **22**, 1220 (1997).

[30] E. Weisstein: *"logistic distribution" from mathworld–a wolfram web resource.* (2005).

[31] R. Napolitano, J. Weiner, C. J. Williams, P. S. Julienne: *Physical Review Letters* **73**, 1352 (1994).

[32] J. L. Bohn, P. Julienne: *Physical Review A* **60**, 414 (1999).

[33] K. M. Jones, P. D. Lett, E. Tiesinga, P. S. Julienne: *Physical Review A* **61**, 012501 (2000).

[34] E. P. Wigner: *Physical Review* **73**, 1002 (1948).

[35] W. Demtröder: *Laser Spectroscopy*: Springer-Verlag, third edn. (2003).

[36] G. Gerber, R. Moller, H. Schneider: *The Journal of Chemical Physics* **81**, 1538 (1984).

[37] N. Boutassetta, A. R. Allouche, M. Aubert-Frécon: *Physical Review A* **53**, 3845 (1996).

[38] J. R. Rubbmark, M. M. Kash, M. G. Littman, D. Kleppner: *Physical Review A* **23**, 3107 (1981).

[39] S. R. Muniz, L. G. Marcassa, R. Napolitano, G. D. Telles, J. Weiner, S. C. Zilio, V. S. Bagnato: *Physical Review A* **55**, 4407 (1997).

[40] E. Merzbacher: *Quantum mechanics*: John Wiley, third edn. (1998).